Force loading explains cell spatial sensing of ligands

Roger Oria[1,2], Tina Wiegand[3,4], Jorge Escribano[5], Alberto Elosegui-Artola[1], Juan Jose Uriarte[2], Cristian Moreno-Pulido[1], Ilia Platzman[3], Pietro Delcanale[1], Lorenzo Albertazzi[1], Daniel Navajas[1,2], Xavier Trepat[1,2,6] José Manuel García-Aznar[5], Elisabetta Ada Cavalcanti-Adam[3,4,*], and Pere Roca-Cusachs[1,2,*]

1 Institute for Bioengineering of Catalonia (IBEC), the Barcelona Institute of Technology (BIST), Barcelona, Spain.
2 University of Barcelona, Barcelona, Spain
3 Max-Planck-Institute for Medical Research, Heidelberg, Germany
4 University of Heidelberg, Heidelberg, Germany
5. Multiscale in Mechanical and Biological Engineering (M2BE), University of Zaragoza, Zaragoza, Spain
6 Institució Catalana de Recerca i Estudis Avançats, Barcelona, Spain

*Corresponding authors. Email: Ada.Cavalcanti-Adam@urz.uni-heidelberg.de, rocacusachs@ub.edu

The density and distribution of extracellular matrix (ECM) ligands, sensed by cells via integrins and integrin-mediated cell adhesions, is a fundamental parameter driving cell response and affecting for instance tumor progression[1] or embryonic development[2]. Previous studies using nanopatterning techniques on rigid glass surfaces have demonstrated that spatial sensing of ECM ligands takes place at the nanoscale, as integrin clustering and subsequent formation of focal adhesions (FAs) was impaired when single integrins bound to ligands were separated by more than a few tens of nm[3-6]. Based on these results, it has been widely hypothesized that a putative adaptor protein of this size could crosslink integrins to the actin cytoskeleton, acting as a molecular ruler to directly sense ligand spacing[3,7-9]. In contrast, here we show that ligand spacing determines cell response by regulating molecular force loading. By using new substrates with tunable rigidity and integrin ligand nano-distribution, we report counterintuitive results showing that (i) increasing ligand spacing promotes -rather than inhibits- the growth of cell-ECM adhesions, and (ii) increasing stiffness beyond a threshold leads to adhesion collapse -rather than growth. Furthermore, disordering ligand distribution drastically increases adhesion growth, but reduces the rigidity threshold for adhesion collapse. Measurements of cellular traction forces and actin flow speeds, combined with an expanded computational molecular clutch model, demonstrate that integrin ligand distribution drives adhesion growth and collapse, and YAP nuclear localization, by determining force loading of integrin-ECM bonds. Our results provide a general framework of how cells sense spatial and physical information at the nanoscale, precisely tuning the range of conditions at which they form adhesions and activate transcriptional regulation. This mechanism may be harnessed by cells in the myriad physiological and pathological processes regulated by mechanical factors and ECM presentation.

To explore cell spatial sensing of ligands, we examined cell response in a wide array of conditions considering not only ligand nano-distribution but also substrate rigidity, which is

by itself a major regulator of adhesions[10]. To this end, we developed a two-step protocol to combine polyacrylamide hydrogels with block co-polymer micelle nanolithography[11]. With this approach, we fabricated hydrogels presenting on their surface nanopatterned quasi-hexagonal arrays of gold nanoparticles (nano-dots) functionalized with the integrin ligand cyclic-RGD (cRGDfk, Fig. 1a). This system allowed single integrin binding per functionalized nano-dot because of steric hindrance[3,8], and control of both nano-dot spacing and substrate rigidity. Due to gel swelling[12], nano-dot spacing was increased in gels with respect to glass surfaces. This swelling was of approximately 20%, and not affected by gel rigidity (Extended Data Fig. 1). We then seeded human breast myoepithelial cells on the substrates, which attached specifically to the nano-dots through the cRGD ligands via α5β1 integrins. Indeed, blocking α5β1 integrins with an antibody, functionalizing nano-dots with a peptide with low affinity for integrin binding (RGE)[13], or functionalizing gels with cRGD in the absence of nano-dots all inhibited cell attachment (Extended Data Fig. 2).

We then analyzed how cells formed adhesions on the substrates as a function of ligand spacing and substrate rigidity. As an initial control, we checked cell behavior on stiff substrates (glass). As expected, cells plated on non-patterned glass substrates (merely coated with a uniform gold layer and functionalized with cRGD) formed long phospho-paxillin (pPax) rich FAs (Fig. 1b,c). On glass nanopatterned substrates with 30 nm spacing, FAs still formed, albeit with a smaller length. In contrast, cells on 50 or 100 nm spaced substrates exhibited only small dotted adhesions. This confirms the previously reported maximum distance between bound integrins for FA formation[3,5], and indicates a length between 30 and 50 nm for a potential molecular ruler in our system. Also as expected and previously described[14], cells seeded on very soft polyacrylamide gels formed small adhesive structures resembling nascent adhesions[15] for both 50 and 100 nm spaced ligands, and only formed FAs above a rigidity threshold of 5 kPa (Fig. 1d,e). However, above this threshold we found several striking behaviors. First, FAs formed on both 50 and 100 nm-spaced gels, even if they did not on glass (Fig. 1b,c). Second, the dependency between FA formation and ligand spacing was reversed from that found on stiff substrates: cells formed longer FAs as ligand spacing increased from 50 to 100 nm. Finally, adhesions seemed to collapse (drastically reduce their length) above a second rigidity threshold, which was of 30 kPa for 100 nm-spaced substrates, and above 150 kPa for 50 nm-spaced substrates. Because FA collapse occurred at a lower rigidity for the higher spacing, this led to a regime (150 kPa) in which FA length increased with decreasing spacing, reproducing the behavior found on glass.

Thus, our results show that there is an optimal rigidity for adhesion formation, which decreases as ligand spacing increases. We then confirmed the generality, validity, and implications of the results in different ways. First, we increased ligand spacing to 200 nm. Confirming the trend, this reduced the optimal rigidity even further to 1.5 kPa (Fig. 1d-e). Second, we checked that quantifying adhesions through GFP-paxillin transfection in live cells rather than pPax stainings in fixed cells, or through overall paxillin recruitment rather than FA length, led to the same trends (Extended Data Fig. 3). Third, we carried out experiments in other cell types (mouse embryonic fibroblasts, human umbilical vein endothelial cells, and MCF10-A breast epithelial cells) and in myoepithelial cells seeded on nano-dots coated with a different ligand, the collagen-mimicking GFOGER peptide[16]. Whereas the specific thresholds varied, the features of adhesion formation and collapse, and their dependency on ligand spacing and substrate rigidity, were maintained in all cases (Extended Data Fig. 4). Finally, we checked the implications of our results beyond FA

formation by analyzing the nuclear localization of the mechanosensitive transcriptional regulator YAP[17], previously shown to correlate with FAs[14]. Indeed, YAP nuclear localization closely mirrored FA length in all cases, showing a rigidity optimum that depended on ligand spacing (Fig. 1f-g).

Our results, showing adhesion formation on 50, 100, and even 200 nm spaced substrates depending on the conditions, are inconsistent with a molecular ruler mechanism, even if we consider that gel deformation could reduce nano-dot spacing. Indeed, whereas cells could potentially pull on neighboring ligands to reduce their distance down to the length of a molecular ruler, this could not explain why on 1.5 kPa substrates FAs form on substrates spaced by 200 nm but not smaller distances. To further discard this hypothesis, we used super-resolution STORM microscopy on 100 nm spaced substrates to image paxillin clusters, which correctly reproduced the expected 100 nm spacing (Extended Data Fig. 5). However, no differences in distances were observed between cells on 30 or 150 kPa substrates, confirming that the increased adhesion formation on the softer 30 kPa substrate was not due to reduced nano-dot spacing caused by gel deformability. The results could not be explained either by differential regulation of cell spreading, which did not correlate well with adhesion formation, particularly on 50 and 100 nm spaced substrates (Extended Data Fig. 3). In contrast, a plausible alternative is regulation by force, previously hypothesized at the theoretical level[18]. It is well supported that mechanical forces play an important role in focal adhesion maturation[19,20], and we previously showed that FA growth in response to rigidity can be explained by force loading in integrins via a molecular clutch mechanism[14,21]. Further, force transmission mediated by a molecular clutch is predicted to depend on ligand density[22,23]. We thus asked whether our results can be explained by a force mechanism regulated by a molecular clutch model.

Our previous model considers a number of myosin motors pulling on an actin filament, generating a rearward actin flow towards the cell center. The substrate is modelled by a set of ECM binding sites (corresponding to the gold nano-dots functionalized with cRGD molecules) connected to a spring representing substrate elasticity. The actin filament is engaged to the substrate through molecular clutches dynamically binding actin to the ECM through integrins and adaptor proteins. When clutches are engaged, they become progressively loaded as myosin motors contract the actin filament. Within adhesions, mechanosensitive adhesion growth is modelled by defining a force threshold in each clutch, which we previously identified as that leading to unfolding of the actin-integrin adaptor protein talin[14]. If any individual clutch surpasses this threshold before disengaging, it triggers a mechanosensing event that grows adhesions by increasing integrin recruitment. As integrins are recruited, the fraction of integrin-bound ligands increases, allowing adhesions to better withstand force. To consider the effects of ligand distribution, we expanded this model in two ways (Fig. 2a, see methods and Extended Data Table 1 for model description and parameters). First, we modelled ECM ligand spacing by using springs to connect ligands not only to the substrate (k_{sub}), but also to each other (k_{link}). In this way and as expected for an elastic substrate, forces applied to one ligand also deform its neighbors. Increasing k_{link} increases this effect on neighbors, modelling the increased mechanical coupling between ligands that would result from reduced spacing. Second, we imposed a maximum integrin recruitment to reflect that integrin clustering cannot grow indefinitely, but will be restricted by integrin packing and the physical size of FAs, stress fibers, and cells themselves.

We then used this model to evaluate the role of ligand spacing. As the number of clutches is reduced and their spacing increases, the force exerted by myosin is distributed among fewer clutches, increasing the force loading of each individual clutch (Fig. 2b). This has no

effect on very soft substrates, where force loading remains too low to reach the force threshold in any case, and adhesions do not grow. However and as rigidity increases, clutches with higher spacing are more likely to reach the force threshold, increasing integrin recruitment. Because FAs grow more, they also reach their maximum recruitment at a lower rigidity. At this point, the increased force loading caused by increased rigidity can no longer be compensated by further recruitment, and the adhesion collapses. Thus, this framework can correctly explain the experimental differences observed. Accordingly, running the computational model with a base set of parameters (Extended Data Table 1) and modifying only the number of ECM ligands (n_l) and their coupling (k_{link}) correctly reproduced the effect of ligand spacing on FAs (Fig. 2c). On 200 nm substrates, we note that experimental effects were even larger than the range that the model could predict.

To further test this model, we verified its predictions on cell-substrate force transmission and actin flows. Regarding force transmission and as previously described[21], our molecular clutch model predicts an initial increase in force transmission with rigidity, followed by a plateau or even slight decrease, followed by a final increase until adhesions and forces collapse. As ligand spacing is decreased, the plateau is shifted to lower rigidities, and lower forces. These predictions were verified by measuring them experimentally using traction force microscopy at all rigidities except 150 kPa, where cell-induced gel displacements were too small to resolve. Whereas agreement with experiments was not exact in all cases, running the model with the same parameters used to model adhesions correctly reproduced the trends and relative differences of measured experimental tractions (Fig. 2d,e). Regarding actin flows, the clutch model predicts that they should be anti-correlated with forces[24], since increased force transmission impairs and slows myosin function. Measured actin flows indeed showed opposite trends to forces in response to both rigidity and ligand spacing, and were correctly reproduced by the model using the same parameters (Fig. 2f,g). Interestingly and unlike force measurements, actin flow measurements were available for 150 kPa substrates, allowing the visualization of the regime inducing adhesion collapse (in 100 nm spacing). As predicted by the model, this collapse resulted in increased actin flows (Fig. 2f,g).

We then explored whether force loading regulated by a molecular clutch could explain cell response not only to overall ligand density, but also ligand distribution. To this end, we used substrates with the same density of nano-dots and the same mean interparticle distance, but with a disordered rather than ordered quasi-hexagonal distribution (Extended Data Fig. 6)[8]. Due to the spatial disorder, the model predicts that force will be distributed less evenly among clutches (Fig. 3a). This leads some clutches to experience high loads, increasing the likelihood of surpassing the mechanosensing force threshold, favoring FA growth, and shifting FA collapse to lower rigidities. This prediction was verified experimentally for substrates with both 50 nm spacing (Fig. 3b,c) and 100 nm spacing (Fig. 3f,g). Indeed, in both cases FA growth at intermediate rigidities was increased drastically, and FA collapse moved to lower rigidities. Of note, and unlike in ordered patterns, disordering the patterned allowed to visualize FA collapse also on 50 nm polyacrylamide substrates. The effect of pattern disorder was successfully modelled by modifying only the parameter representing ligand spacing (k_{link}), to which we assigned not a constant value for all ligands, but a distribution of random values centered on a mean (Fig. 3c,g). In terms of force transmission, the model predicts that due to the increased adhesion formation, disorder eliminates the plateau observed at intermediate rigidities, leading to a monotonic force increase with rigidity up until FA collapse. This was verified experimentally, and was modelled successfully with the same parameters (Fig. 3d,e, h,i). Importantly, disordering the pattern on 100 nm substrates shifted the onset of FA collapse to a rigidity low enough (30 kPa) to measure

force transmission. This allowed us to verify the prediction that FA collapse at high rigidities is also associated with a decrease in force transmission (Fig. 3i).

Finally, we verified a fundamental hypothesis of the model: that FA collapse at high rigidities is due to excessive loading of integrin-ECM bonds, which can no longer be compensated with adhesion growth. This hypothesis leads to the very counter-intuitive prediction that in this "collapsed" regime, decreasing force loading (for instance by impairing myosin function) should lead to adhesion growth. To confirm this, we seeded cells on rigid 150 kPa gels with 100 nm spaced nano-dots, thereby generating collapsed FAs. Then, we treated cells with the myosin inhibitor blebbistatin after 1h of seeding. As predicted, using a mild concentration of blebbistatin (5 μM) resulted in FA growth (Fig 4a-c) as compared with the control condition, effectively putting cells in the intermediate force loading regime where FA growth is favored (Fig. 4a). Also as expected, using a higher concentration of blebbistatin (15μM) reversed the effect, as force loading was disrupted enough to bring cells to the low rigidity regime where FAs are also impaired (Fig. 4a-c). Conversely, increasing myosin contractility using calyculin A[25] in cells with the largest adhesions (100 nm spacing, 30 kPa) brought cells to the collapsed regime, decreasing adhesion length (Fig. 4d-f).

The field of cell-matrix adhesion is very mature, and several studies have addressed how adhesions are regulated by molecular interactions[26-28] and physical signals[14,19,29,30]. In this regard, there is a wide consensus that cells respond to increases in both stiffness and ligand density by promoting adhesion growth[3,4,14,21,31]. Strikingly, here we find the opposite behavior in response to both factors. This behavior is explained not by a distance sensing mechanism per se but by regulation of molecular force loading, within a predictive model that integrates the effects of stiffness, ligand distribution, and contractility. Resulting cell response includes the surprising feature of adhesion collapse under high load, which can explain previous results on stiff substrates showing how ligand molecular length regulates adhesion stability[32], and how increasing ligand spacing renders adhesions unstable [7,18] and unable to sustain large forces on integrins over time[33]. Our results provide a general framework of how cells sense spatial and physical information at the nanoscale, precisely tuning the range of conditions at which they form adhesions and activate transcriptional regulation via YAP. This mechanism may be harnessed by cells in the myriad physiological and pathological processes regulated by mechanical factors and ECM presentation.

References

1 Lu, P., Weaver, V. M. & Werb, Z. The extracellular matrix: a dynamic niche in cancer progression. *The Journal of cell biology* **196**, 395-406, doi:10.1083/jcb.201102147 (2012).

2 Daley, W. P., Peters, S. B. & Larsen, M. Extracellular matrix dynamics in development and regenerative medicine. *Journal of cell science* **121**, 255-264, doi:10.1242/jcs.006064 (2008).

3 Arnold, M. *et al.* Activation of integrin function by nanopatterned adhesive interfaces. *Chemphyschem : a European journal of chemical physics and physical chemistry* **5**, 383-388, doi:10.1002/cphc.200301014 (2004).

4 Cavalcanti-Adam, E. A. *et al.* Lateral spacing of integrin ligands influences cell spreading and focal adhesion assembly. *European journal of cell biology* **85**, 219-224, doi:10.1016/j.ejcb.2005.09.011 (2006).

5 Altrock, E., Muth, C. A., Klein, G., Spatz, J. P. & Lee-Thedieck, C. The significance of integrin ligand nanopatterning on lipid raft clustering in hematopoietic stem cells. *Biomaterials* **33**, 3107-3118, doi:10.1016/j.biomaterials.2012.01.002 (2012).

6 Amschler, K., Erpenbeck, L., Kruss, S. & Schon, M. P. Nanoscale integrin ligand patterns determine melanoma cell behavior. *ACS nano* **8**, 9113-9125, doi:10.1021/nn502690b (2014).

7 Cavalcanti-Adam, E. A. *et al.* Cell spreading and focal adhesion dynamics are regulated by spacing of integrin ligands. *Biophysical journal* **92**, 2964-2974, doi:10.1529/biophysj.106.089730 (2007).

8 Huang, J. *et al.* Impact of order and disorder in RGD nanopatterns on cell adhesion. *Nano Lett.* **9**, 1111-1116, doi:10.1021/nl803548b (2009).

9 Schvartzman, M. *et al.* Nanolithographic control of the spatial organization of cellular adhesion receptors at the single-molecule level. *Nano letters* **11**, 1306-1312, doi:10.1021/nl104378f (2011).

10 Plotnikov, S. V., Pasapera, A. M., Sabass, B. & Waterman, C. M. Force fluctuations within focal adhesions mediate ECM-rigidity sensing to guide directed cell migration. *Cell* **151**, 1513-1527, doi:10.1016/j.cell.2012.11.034 (2012).

11 Lohmuller, T. *et al.* Nanopatterning by block copolymer micelle nanolithography and bioinspired applications. *Biointerphases* **6**, MR1-12, doi:10.1116/1.3536839 (2011).

12 Ahmed, E. M. Hydrogel: Preparation, characterization, and applications: A review. *Journal of advanced research* **6**, 105-121, doi:10.1016/j.jare.2013.07.006 (2015).

13 Hersel, U., Dahmen, C. & Kessler, H. RGD modified polymers: biomaterials for stimulated cell adhesion and beyond. *Biomaterials* **24**, 4385-4415 (2003).

14 Elosegui-Artola, A. *et al.* Mechanical regulation of a molecular clutch defines force transmission and transduction in response to matrix rigidity. *Nat. Cell Biol.* **18**, 540-548, doi:10.1038/ncb3336 (2016).

15 Lawson, C. *et al.* FAK promotes recruitment of talin to nascent adhesions to control cell motility. *The Journal of cell biology* **196**, 223-232, doi:10.1083/jcb.201108078 (2012).

16 Emsley, J., Knight, C. G., Farndale, R. W., Barnes, M. J. & Liddington, R. C. Structural basis of collagen recognition by integrin alpha2beta1. *Cell* **101**, 47-56, doi:10.1016/S0092-8674(00)80622-4 (2000).

17 Dupont, S. *et al.* Role of YAP/TAZ in mechanotransduction. *Nature* **474**, 179-183, doi:10.1038/nature10137 (2011).

18 de Beer, A. G. *et al.* Force-induced destabilization of focal adhesions at defined integrin spacings on nanostructured surfaces. *Physical review. E, Statistical, nonlinear, and soft matter physics* **81**, 051914, doi:10.1103/PhysRevE.81.051914 (2010).
19 Riveline, D. *et al.* Focal contacts as mechanosensors: externally applied local mechanical force induces growth of focal contacts by an mDia1-dependent and ROCK-independent mechanism. *The Journal of cell biology* **153**, 1175-1186 (2001).
20 Wolfenson, H., Bershadsky, A., Henis, Y. I. & Geiger, B. Actomyosin-generated tension controls the molecular kinetics of focal adhesions. *Journal of cell science* **124**, 1425-1432, doi:10.1242/jcs.077388 (2011).
21 Elosegui-Artola, A. *et al.* Rigidity sensing and adaptation through regulation of integrin types. *Nature materials* **13**, 631-637, doi:10.1038/nmat3960 (2014).
22 Bangasser, B. L. & Odde, D. J. Master equation-based analysis of a motor-clutch model for cell traction force. *Cellular and molecular bioengineering* **6**, 449-459, doi:10.1007/s12195-013-0296-5 (2013).
23 Bangasser, B. L., Rosenfeld, S. S. & Odde, D. J. Determinants of maximal force transmission in a motor-clutch model of cell traction in a compliant microenvironment. *Biophys. J.* **105**, 581-592, doi:10.1016/j.bpj.2013.06.027 (2013).
24 Chan, C. E. & Odde, D. J. Traction dynamics of filopodia on compliant substrates. *Science* **322**, 1687-1691, doi:10.1126/science.1163595 (2008).
25 Peterson, L. J. *et al.* Simultaneous stretching and contraction of stress fibers in vivo. *Mol. Biol. Cell.* **15**, 3497-3508, doi:10.1091/mbc.E03-09-0696 (2004).
26 Humphries, J. D. *et al.* Vinculin controls focal adhesion formation by direct interactions with talin and actin. *The Journal of cell biology* **179**, 1043-1057, doi:10.1083/jcb.200703036 (2007).
27 Kanchanawong, P. *et al.* Nanoscale architecture of integrin-based cell adhesions. *Nature* **468**, 580-584, doi:10.1038/nature09621 (2010).
28 Choi, C. K. *et al.* Actin and alpha-actinin orchestrate the assembly and maturation of nascent adhesions in a myosin II motor-independent manner. *Nature cell biology* **10**, 1039-1050, doi:10.1038/ncb1763 (2008).
29 Prager-Khoutorsky, M. *et al.* Fibroblast polarization is a matrix-rigidity-dependent process controlled by focal adhesion mechanosensing. *Nature cell biology* **13**, 1457-1465, doi:http://www.nature.com/ncb/journal/v13/n12/abs/ncb2370.html#supplementary-information (2011).
30 Oakes, P. W., Beckham, Y., Stricker, J. & Gardel, M. L. Tension is required but not sufficient for focal adhesion maturation without a stress fiber template. *The Journal of cell biology* **196**, 363-374, doi:10.1083/jcb.201107042 (2012).
31 Engler, A. *et al.* Substrate compliance versus ligand density in cell on gel responses. *Biophysical journal* **86**, 617-628, doi:10.1016/S0006-3495(04)74140-5 (2004).
32 Pallarola, D. *et al.* Interface Immobilization Chemistry of cRGD-based Peptides Regulates Integrin Mediated Cell Adhesion. *Advanced functional materials* **24**, 943-956, doi:10.1002/adfm.201302411 (2014).
33 Liu, Y. *et al.* Nanoparticle tension probes patterned at the nanoscale: impact of integrin clustering on force transmission. *Nano letters* **14**, 5539-5546, doi:10.1021/nl501912g (2014).

Acknowledgments: This work was supported by the Spanish Ministry of Economy and Competitiveness (BFU2015-65074-P to X.T., BFU2016-79916-P and BFU2014-52586-REDT to P.R.-C., DPI2015-64221-C2-1-R to J.M.G.-A., PI14/00280 to D.N.), the European Commission (Grant Agreement SEP-210342844 to X.T., and P.R.-C.), the Generalitat de Catalunya (2014-SGR-927), the European Research Council (CoG-616480 to X.T. and StG 306571 to J.M.G.-A.), Obra Social "La Caixa", Fundació la Marató de TV3 (project 20133330 to P.R.-C.), and the EMBO Young Investigator Programme. R.O. and A.E.-A. were supported respectively by a Juan de la Cierva Fellowship (Spanish Ministry of Economy and Competitiveness) and a FI fellowship (Generalitat de Catalunya). We thank the members of the P.R.-C. and X.T. laboratories, P. Oakes, and J. Spatz for technical assistance and discussions.

Author contributions: R.O. and P.R.-C. conceived the study, R.O., L.A., D.N., X.T., A.C.-A., and P.R.-C. designed the experiments, R.O., T.W., A.E-A., J.J.U., I.P., and P.D. performed the experiments, J.E., C.M.-P., J.M.G.-A., and P.R.-C. carried out the theoretical modelling, and R.O. and P.R-C. wrote the manuscript. All authors commented on the manuscript and contributed to it.

Author information: Reprints and permissions information is available at www.nature.com/reprints. The authors declare no competing financial interests. Readers are welcome to comment on the online version of the paper. Correspondence and requests for materials should be addressed to P.R.-C. (rocacusachs@ub.edu) and A.C.-A. (Ada.Cavalcanti-Adam@urz.uni-heidelberg.de).

Figures

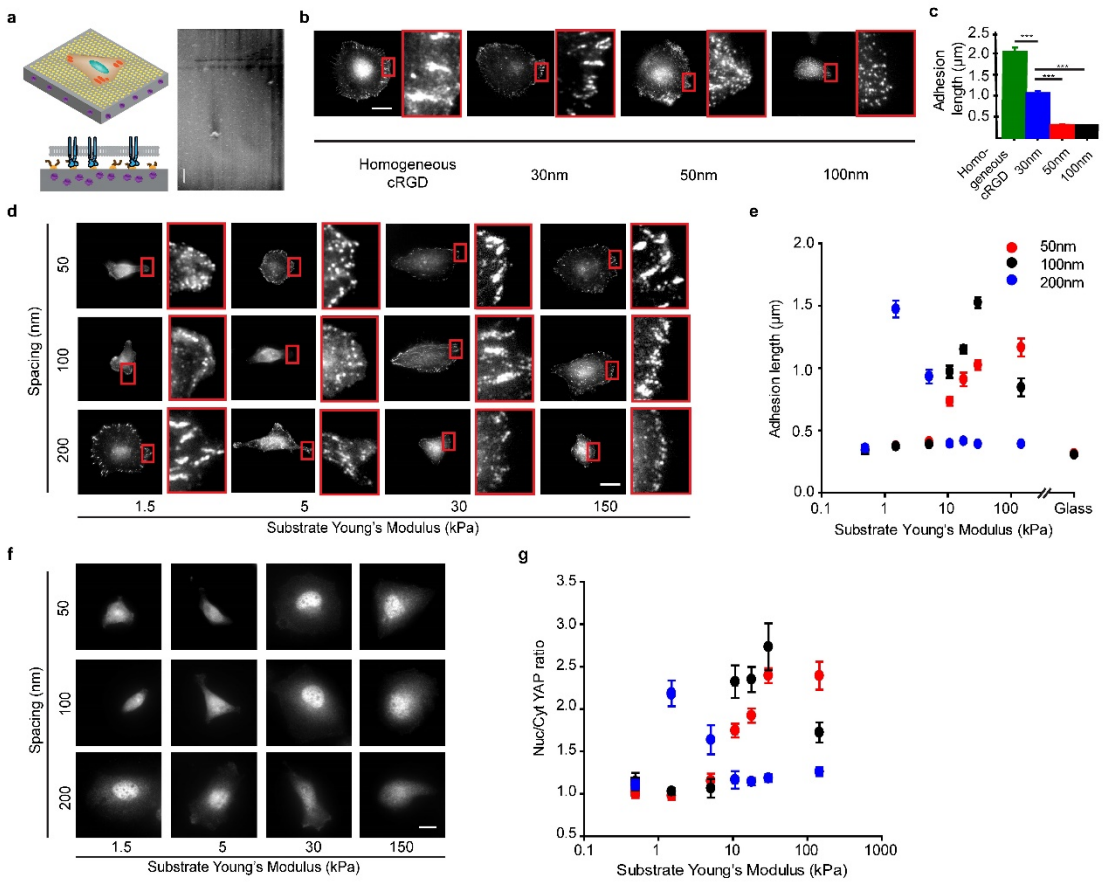

Fig. 1. Increasing ligand spacing promotes adhesion growth for intermediate rigidities and collapse for high rigidities. (a) (Top) Scheme of the nanopatterned polyacrylamide substrates showing gold nano-dots (yellow) on top of poly-acrylamide gels with embedded fluorescent beads (purple). (bottom) Inset showing the spatial configuration of the integrin-ECM bonds on the quasi-hexagonal pattern of nano-dots coated with cRGD ligands (shown in black). (Right) Scanning electron micrograph of a 100 nm pattern on a polyacrylamide gel (2 independent experiments). (b) Staining of phospho-paxillin adhesions of cells seeded on glass substrates coated with either a homogeneous layer of cRGD or quasi-hexagonal distributed cRGD ligands (30nm, 50nm and 100nm spacing). Zoomed regions on the right of the images correspond to rectangles marked in red in the main image. (c) Corresponding quantification of FA length (at least 3 FA for n=12 cells per condition for two independent experiments) (***, p<0.001, one-way ANOVA) (d) Staining of phospho-paxillin adhesions of cells seeded on polyacrylamide substrates ranging from 0.5kPa to 150kPa with either 50, 100 or 200nm spaced nano-dots. (e) Corresponding quantification of FA length (at least 3 FA for n=10/10/11, 10/12/11, 10/11/11, 10/10/11, 12/11/11, 10/10/11, 11/11/11, 12,12,- cells for 50/100/200 nm substrates and increasing rigidity, two independent experiments). The effect of both rigidity and spacing was significant ($p < 0.05$, two-way ANOVA). (f) YAP stainings in cells seeded on polyacrylamide substrates ranging from 0.5kPa to 150 kPa with either 50nm, 100nm and 200nm spaced nano-dots (g) Corresponding quantification of nuclear/cytosolic YAP ratio (n=15 cells per condition, two independent experiments). Scale

bars, 20 μm. The effect of both rigidity and spacing was significant ($p < 0.05$, two-way ANOVA). Error bars, mean ± s.e.m.

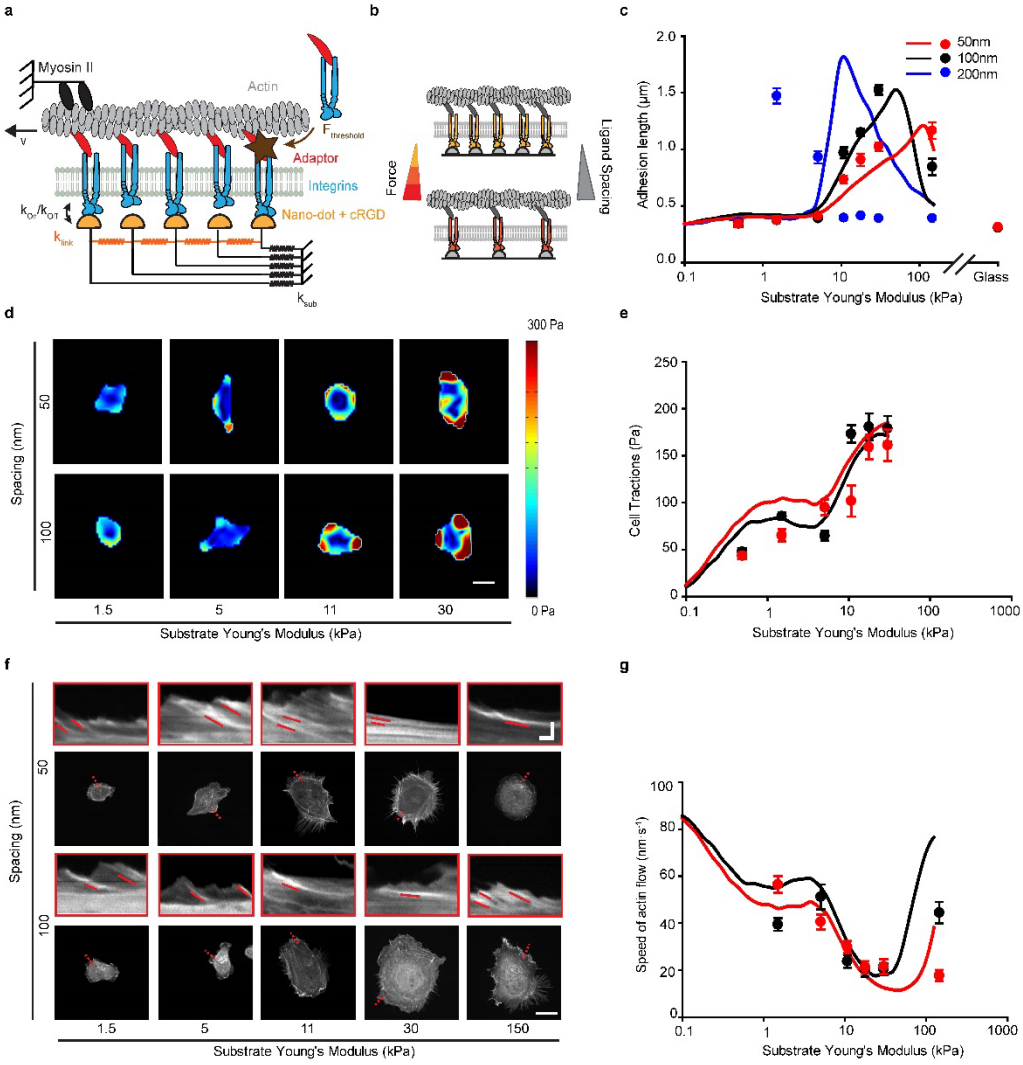

Fig. 2. A molecular clutch model explains cell response to ligand spacing. (a) Scheme of the molecular clutch model. Myosin motors (black) pull on actin (grey) with a velocity v, which exerts a force on a set of parallel clutches (formed by adaptor proteins, red, and integrins, blue) which dynamically bind and unbind cRGD ligands (yellow) with on- and off-rates k_{on} and k_{off}. Mechanosensitivity is introduced by setting a force threshold $F_{threshold}$ in each clutch that triggers further integrin recruitment when surpassed (event symbolized by brown star). The elastic substrate is represented by springs connecting ligands to the substrate (k_{sub}, black) and to each other (k_{link}, orange). (b) Scheme depicting the effect of ligand spacing on clutch forces. (c) Model predictions (solid lines) and experimental average values (same data as fig. 1e) for adhesion length as rigidity increases for 50nm, 100nm and 200nm spaced substrates. Model parameters changed were n_l (180 for 50 nm, 130 for 100 nm and 5 for 200nm) and the ratio k_{link}/k_{sub} (10 for 50 nm, 5 for 100 nm and 3 for 200nm). (d) Examples of cell tractions exerted on 1.5, 5, 11 and 30kPa substrates for 50 and 100nm spacing. (e) Corresponding model predictions (solid lines) and experimental average values for cell tractions (n=13/13, 11/16, 11/19, 16/13, 13/16, 13/14 cells for 50/100 nm substrates and increasing rigidity, two independent experiments). (f) Examples of LifeAct-GFP

transfected cells plated on substrates with increasing rigidity. Insets are kymographs showing the movement of actin features along the lines marked in red. The slope of the traces created by the features (marked with dashed lines) was used to calculate actin speed. (g) Corresponding model predictions (solid lines) and experimental average values for actin speed (at least 3 traces for n=7/9, 9/9, 11/9, 8/7, 8/7, 9/9 cells for 50/100 nm substrates and increasing rigidity, two independent experiments). Scale bars, 20 μm in the main images and 20 s/2μm (x=y axes) in the kymographs. Error bars, mean ± s.e.m.

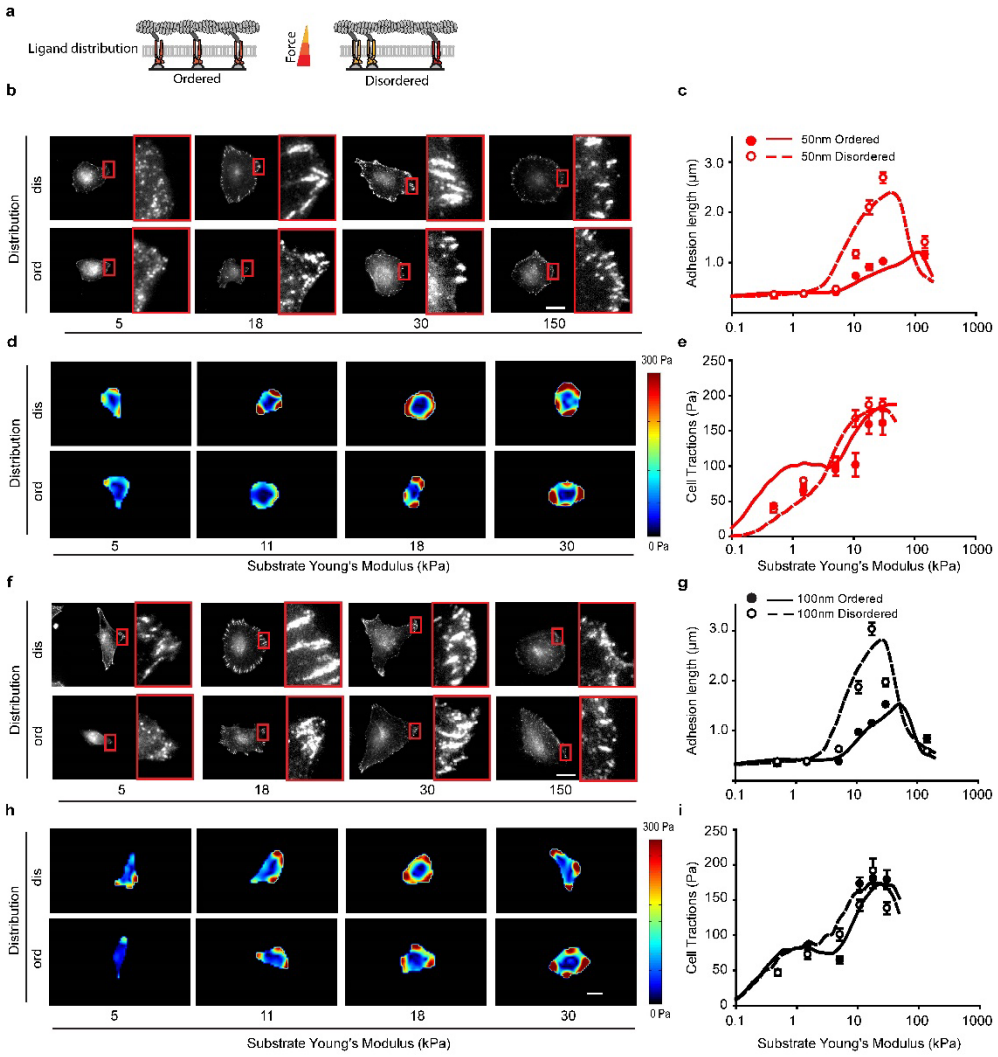

Fig. 3. Ligand disorder promotes adhesion growth as predicted by the molecular clutch model. (a) Scheme showing the effect of ligand disorder on clutch force. (b) Stainings of phospho-paxillin adhesions for cells seeded on 5, 18, 30 and 150kPa substrates with either ordered or disordered 50nm spacing. (c) Corresponding model predictions (lines) and experimental average values for adhesion length (at least 3 FA for n=10/10, 10/10, 10/10, 11/10, 11/12, 11/10, 11/11 cells for disordered/ordered conditions and increasing rigidity, two independent experiments). Differences between ordered and disordered conditions were significant ($p < 0.05$, two-way ANOVA). (d-e) For the same 50 nm substrates, (d) examples of cell tractions and (e) corresponding model predictions (solid lines) and experimental average traction values (n=14/13, 12/11, 12/11, 19/16, 16/13, 21/13 cells for disordered/ordered conditions, two independent experiments). Differences between ordered and disordered conditions were significant ($p < 0.05$, tow-way ANOVA). (f-g) For 100 nm substrates, (f) stainings of phospho-paxillin adhesions for ordered and disordered substrates and (g) corresponding model predictions (lines) and experimental average traction values (at least 3 FA for n=10/10, 10/12, 10/11, 11/10, 12/11, 11/10, 11/11 cells for disordered/ordered conditions, two independent experiments). (h-i) For the same 100 nm

substrates, (h) examples of cell tractions and (i) corresponding model predictions (solid lines) and experimental average traction values (n=12/13, 15/16, 18/19, 14/13, 11/16, 15/14 cells for disordered/ordered conditions, two independent experiments). Scale bars, 20 μm. Error bars, mean ± s.e.m.

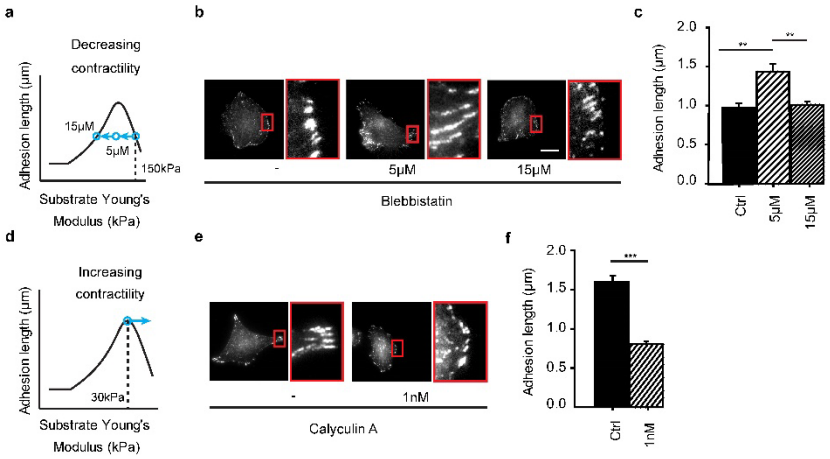

Fig. 4. Myosin contractility regulates adhesion growth according to model predictions. (a) Scheme showing how progressively decreasing contractility in cells with collapsed adhesions (150 kPa, 100 nm spacing) should first bring adhesion length to its maximum, and then decrease it again. (b) Stainings of phospho-paxillin adhesions for control and blebbistatin treated cells (5 and 15 µM) on 150 kPa substrates with 100nm spacing. (c) Corresponding quantification of FA length (at least 3 FA for n=14 cells per condition, two independent experiments). (d) Scheme showing how increasing contractility in cells with maximum adhesions (30 kPa, 100 nm spacing) should decrease adhesion length. (e) Stainings of phospho-paxillin adhesions for control and calyculin A treated cells on 30 kPa substrates with 100nm spacing. (f) Corresponding quantification of FA length (at least 3 FA for n=15 cells per condition, two independent experiments, two-tailed student's t-test). Scale bars, 20 µm. **, p< 0.01, ***, p<0.001. Error bars, mean ± s.e.m.

METHODS

Preparation of nanopatterned substrates on glass surfaces. Nanopatterned substrates were prepared as previously described[3,4,7]. Briefly, polystyrene(x)-*b*-poly(2-vinylpyridine)(y) diblock copolymers (PolymerSource Inc.) and Polystyrene standard (Alfa Aesar) were dissolved in toluene and stirred for 24 h at room temperature. Different compositions were used to generate ordered and disordered substrates with different spacing, see Extended Data Table 2. $HAuCL_4{\cdot}3H_20$ (Sigma–Aldrich) was added to the micellar solutions with a specific loading parameter defined as $L = n[\mathrm{HAuCL4}]/\mathrm{n[P2VP]}$. For disordered structures the micellar gold solution was mixed with a polystyrene solution in a 1:1 ratio. 10 µl of the solution were spincoated (WS-400A-6NPP/Lite, Laurell Technologies Cooperation) on 12 mm round coverglasses, previously cleaned with piranha solution. Samples were treated with oxygen plasma (TePla 100-E, 0.4 mbar, 150 W, 10 min) to remove the polymer matrix.

Transfer of nanopatterns to polyacrylamide gels. Nanostructured glass surfaces were activated with UV for 30 min, incubated in 10 mM N, N´-bis-(acryloyl)cystamine (Sigma-Aldrich) in EtOH in the dark for 1h and washed thoroughly with pure EtOH. Next, nanostructured surfaces were dried with N2. Polyacrylamide gels were prepared as previously described[21]. Briefly, glass-bottom dishes were incubated with a solution of acetic acid, 3-(Trimethoxysilyl)propyl methacrylate (Sigma), and ethanol (1:1:14), washed three times with 96% ethanol. A solution containing 0.5% ammonium persulphate, 0.2% tetramethylethylenediamine (Sigma), 2% fluorescent 200nm red carboxylated nanobeads (Invitrogen), was mixed with different concentrations of acrylamide and bis-acrylamide to make gels of different rigidities (see Extended Data Table 3). 10 µl of this solution were then placed on the centre of glass-bottom dishes and covered with 12 mm nanostructured surfaces. After 20 min of gel polymerization, hydrogels were soaked in PBS and incubated in the oven for 72h at 37º, allowing them to swell. Hydrogels were then stabilized at room temperature and the patterned glass surfaces were removed carefully from the hydrogel. Then, hydrogels with nanopatterned nano-dots were gently washed with PBS and subsequently incubated with 25µM cRGD-thiol (cyclo [Arg-Gly-Asp-D-Phe-Lys(Ahx-Mercaptopropionic Acid), PCS-31062-PI, Peptides International) at room temperature for 4 h. Afterward, cRGD conjugated nanopatterned hydrogels were washed to remove unbound peptides for 5 times (for at least 10min each time) prior cell seeding. For GFOGER experiments, after removing the glass surfaces, gels were incubated with 1mM of the hetero-bifunctional linker 11-mercaptoundecanoyl N-hydroxysuccinimide ester (MU-NHS) (Prochimia) for 3 hours, afterwards 1uM of GFOGER peptide was incubated overnight. GFOGER conjugated nanopatterned hydrogels were washed to remove unbound peptides for 5 times (for at least 10min each time) prior to cell seeding.

Substrate characterization with scanning electron microscopy (SEM) and Cryo-SEM. Nanostuctured surfaces were sputtered with carbon (Low Vacuum Coater EM ACE200, Leica) and imaged by SEM (Leo1530, Zeiss) with in-lense detector and 5 kV acceleration voltage at working distances between 9 and 11 mm. Polyacrylamide hydrogels with embedded gold nano-dots were vitrified, mounted in a liquid nitrogen-cooled stage and transferred to a freeze fracture system (EM BAF060, Leica). Samples were heated to -90 °C, kept in vacuum for 45 min to sublimate the water at the interfaces, and coated with carbon. Samples were further transferred to the Cryo-SEM (Ultra 55 FE-SEM, Zeiss) by an evacuated liquid nitrogen-cooled shuttle (BAL-TECH VLC 100). Images were recorded at low-temperature conditions (T=-130 ± 5 °C) and low acceleration voltages of 1-1.5 kV because of the low conductivity of the samples with a working distance of 3 mm. Resulting

Electron micrographs were analyzed in ImageJ (National Insitutes of Health) by measuring the distances between a gold nanoparticle and its k-nearest neighbors (k=6 for ordered nanostructures, 4<k<8 for disordered nanostructures) for at least 300 particles of ≥2 individual nanostructures per condition.

Cell culture and reagents. Human breast myoepithelial immortalized cell lines were described previously[21,34], and cultured in Hams-F12 (Sigma, N4888) media supplemented with 10% FBS, 1% penicillin streptomycin, Hydrocortisone (1µg/ml), EGF (10ng/ml) and Insulin (5µg/ml). Human umbilical vein endothelial cells were purchased from Lonza (CC-2517) and cultured in EGM-2 (Lonza CC-4176). Mouse Embryonic fibroblasts were described previously[35], and cultured in DMEM (LifeTechnologies, 41965-039) media supplemented with 10% FBS, 1% penicillin streptomycin. Mammary epithelial cells (MCF10A) were purchased from ATCC and cultured in DMEM-F12 (LifeTechnologies, 21331-020) with 5% horse serum and 1% penicillin streptomycin, EGF (20ng/ml), Hydrocortisone (0.5µg/ml), Cholera toxin (100ng/ml), insulin 10 (µg/ml). Myoepithelial cells used throughout the manuscript were authenticated in their lab of origin through expression of Integrin β4 , P-cadherin, cytokeratin 17, and desmoglein 3. Other cell lines (used only to verify the generality of our findings) were not authenticated. For all experiments, cells were gently washed with PBS twice, trypsinized, and resuspended in media without FBS. After centrifugation, cells were seeded on hydrogels with media without FBS. To block α5β1 integrins, cells were incubated with an α5β1 integrin blocking antibody (30ug/ml, clone JBS5 - MAB1969, Millipore) for 30min before seeding. Cell attachment was evaluated 1h after seeding. For blebbistatin experiments, cells were treated with indicated concentrations of blebbistatin (CalBiochem) for 30 min. For Calyculin A experiments, cells were treated with the indicated concentration (merckmillipore) for 30 min. All cells tested negative for mycoplasma contamination.

Traction-force measurements. Traction force measurements were carried out as previously described[14,21]. Briefly, cells seeded on gels were placed on an inverted microscope (Nikon Eclipse Ti). Single cells were tracked for 3 h, while we acquired phase-contrast images of the cells and fluorescence images of the embedded nanobeads using a 40x objective. Then, cells were trypsinized, and an image of bead position in the relaxed state of the gel was acquired. By comparing bead positions with and without cells, a map of gel deformations caused by cells was first obtained using custom particle-imaging-velocimetry software. Then, after assuming that gel displacements were caused by forces exerted by cells in the cell gel contact area, the corresponding map of cell forces was calculated using a previously described Fourier transform algorithm. The average forces per unit area exerted by each cell were then calculated. Force measurements for each cell were taken once per hour during the measurement, and the average value for all time measurements was used.

Rearward-flow measurements. To measure actin rearward flow, cells were transfected with LifeAct-GFP using jetPRIME transfection kit (Polyplus transfection) 1 day before measurements. Cells were then plated on gels of varying rigidity, and imaged every second for 2 min with 60x oil immersion objective (N.A. 1.40) with spinning-disc confocal microscopy (Andor). For each cell, kymographs were obtained at the cell periphery, and actin speed was measured from the slope of actin features observed in the kymographs. In cells plated on

0.5 kPa gels, actin features were so diffuse that no reliable slopes could be measured in kymographs.

Immunostaining and adhesion quantification. For fluorescence staining of cell-substrate adhesions, cells were fixed with 4% paraformaldehyde, permeabilized with 0.1% Triton X-100, and labelled first with primary antibody against either phospho-paxillin (Cell Signaling 2541S, 1:50 dilution) or YAP (clone 63.7 produced in mouse, Santa Cruz catalogue no. sc-101199, 1:200 dilution) for 1 h at room temperature, and then with anti-rabbit or anti-mouse Alexa-conjugated secondary antibody (Invitrogen) for 1 h at room temperature. Fluorescence images were then acquired with a 60x oil immersion objective (NA 1.40) using a Nikon Eclipse Ti microscope. To quantify adhesion lengths, FAs were identified manually and their length was measured. To provide an alternative quantification unbiased by the identification of specific structures, we also quantified the average intensity of phospho-paxillin staining in regions at the cell edge containing both adhesions and surrounding areas, as described previously[21]. Then, we subtracted the background intensity value calculated from neighboring cell areas lacking adhesions. The measured trends as a function of both stiffness and ligand density were the same in both quantifications. The degree of YAP nuclear localization was assessed by calculating the ratio between YAP fluorescence in the nuclear region and the cytoplasmic region immediately adjacent. Nuclear and cytoplasmic regions were previously determined by co-staining the nucleus with Hoechst 33342.

Measurements of gel stiffness. The stiffness (Young's modulus) of polyacrylamide gels was measured by atomic force microscopy as previously described[36]. Briefly, measurements were made with a custom-built atomic force microscope attached to an inverted optical microscope (Nikon TE200). Silicon nitride pyramidal tips with an effective half-angle θ of 20° and a nominal spring constant of k = 0.01–0.03 N m^{-1} were used (MLCT, Bruker). The actual spring constant was calibrated by thermal tuning using the simple harmonic oscillator model[37] . The Young's modulus was measured by recording 10 force-displacement curves with a peak-to-peak amplitude of 6 µm and a frequency of 1 Hz. Three points near the gel centre were selected in each gel, separated 5 µm from each other. For each stiffness, ≥6 gels produced in two batches were measured. To compute the Young's modulus (E), the Hertz model equation for pyramidal tips was fitted to the force-displacement curves. The equation was fitted for an effective indentation of 1,000 nm for all rigidities except 150kPa, where 500nm was used.

STORM imaging and distance assessment. To perform direct STORM (dSTORM) imaging, immunostained cells on gels of different stiffness were mounted on a 24mm x 24 mm glass coverslip using Vectashield (H-1000). For image acquisitions, the samples were flipped and placed on the microscope's sample holder. This allowed the excitation light to pass through the optically-matched layer of Vectashield mounting medium and to be focused on the focal adhesions located at the interface between cells and gel substrate. F8811 spheres (Life Technology) on the gel surface allowed for the correction of the mechanical drift during acquisition while the mounting medium allowed for the photoswitching of the fluorophores necessary to perform dSTORM. dSTORM images were acquired using a Nikon N-STORM 4.0 system configured for total internal reflection fluorescence (TIRF) imaging. Alexa647-labelled secondary antibodies were imaged by means of a 647 nm laser (160 mW) while the F8811 spheres were imaged by means of a 488 nm laser (80mW). No activation UV light was employed. Fluorescence was collected using a Nikon 100X, 1.49 NA oil

immersion objective and passed through a quad-band pass dichroic filter (97335 Nikon). Images were acquired onto a 128x128 pixel region (pixel size 0.16 μm) of a Hamamatsu ORCA- Flash 4.0 camera at 5 ms integration time. A total of 50,000 frames were acquired for the 647 channel. Every 100 imaging frames, one image of the 488 channel was acquired to perform drift correction. STORM images were analyzed with the STORM module of the NIS element Nikon software. The NIS elements Nikon software generates a list of localizations by Gaussian fitting of blinking dyes in the acquired movie of conventional microscopic images. To avoid overcounting, blinkings detected in consecutive frames are counted as single by the software. For pattern analysis of focal adhesions, the lists of localizations corresponding to focal adhesion regions (size about 2.5 μm) were imported and converted in binary images with a pixel size of 3 nm, using a custom Matlab script. Then, binary images were dilated, and clusters identified. A threshold radius was set to discard single blinks not belonging to the cluster. A first analysis of the patterns was then performed with a previously developed Matlab script[38,39] to calculate the pair-correlation functions of cluster patterns up to distances of 900nm from the identified clusters. Additionally, the centroid of each cluster was identified and the distance of the nearest neighbor was calculated with a custom Matlab script.

Statistical analysis. Data reported throughout the manuscript are mean ± standard error of the mean (s.e.m.). Statistical analyses were done with two-tailed student's t-test when two cases were compared, and with analysis of variance (ANOVA) tests when more cases were analyzed. If data did not meet normality criteria, equivalent non-parametric tests were employed. No statistical methods were used to predetermine sample size.

Availability of data and of computational model and code. Details on the computational model and its implementation are provided below. The data that support the findings of this study, and the Matlab code employed to generate the model is available on request to rocacusachs@ub.edu.

Molecular clutch model implementation.

Base model. The implementation of the molecular clutch model was based on a model previously described in detail[21], which was in turn based in previous implementations[22-24]. Briefly, the model considers a given number of myosin molecules n_m pulling on an actin fiber, which in the absence of load contracts at a rearward speed v_u. The substrate is represented by a set of ligands n_l (cRGD functionalized gold nano-dots in this case) connected to springs representing substrate elasticity. The actin fiber binds to the ligands dynamically through molecular clutches which represent the adaptor protein-integrin complex. Those clutches have characteristic on- and off- rates k_{ont} and k_{off}. k_{off} (in units of s^{-1}) depends on force as a catch bond, which we modelled according to the experimental values of fibronectin-α5β1 bonds previously reported[40]. k_{ont} (in units of $s^{-1}\mu m^2$) is the true on-rate of each ligand, which must be multiplied by the available density Page of integrins (d_{int}) to provide an effective on-rate with units of s^{-1}. The model is implemented as a Montecarlo stochastic simulation which starts with all clutches disengaged, and actin flowing freely. As the simulation progresses and clutches engage they pull on the substrate, loading force on the clutches and affecting k_{off}. Additionally, force exerted by the substrate on actin slows the myosin motors linearly, which are assumed to stall and stop completely at a force of $n_m \cdot F_m$, where F_m is the stall force of an individual motor. To model mechanosensitive adhesion growth (reinforcement), if individual clutches exceed a given force threshold $F_{threshold}$ before disengaging, integrins are recruited. This is implemented by increasing d_{int} by a factor d_{add}. In previous work, we

identified this mechanosensitive event as the unfolding of talin[14]. The simulation is run for 100 s with time steps of 2 ms, and run 20 times per condition to obtain average results.

Model expansion. To the model described previously and summarized above, we added two main features to model the effect of substrate spacing and distribution. First, we simply introduced a maximum value for d_{int} (d_{intmax}) to model that integrin recruitment has a physical limit. To calculate a parameter predictive of adhesion size, in simulations we then multiplied d_{int} by the fraction of bound clutches. To compare it with experimental adhesion lengths, we scaled model predictions for cells on 100 nm substrates as a function of stiffness to fall between the maximum and minimum experimental values. All other conditions were scaled by using the same 100 nm reference to retain the relative differences predicted by the model. The second and most important novel feature was an improvement of the elastic characterization of the system. In our previous models, the substrate was modelled simply as a set of ligands connected to each other with a rigid rod, which was in turn connected to an elastic spring. Whereas this effectively modelled substrate stiffness, deformation in all ligands was always the same: it did not allow to model the elastic coupling between ligands, i.e. the fact that a force applied to a ligand will deform neighboring ligands to a lesser extent as the distance increases. To introduce this, we modelled the substrate not as a single spring, but as a network of springs, where each ligand had a spring connecting it to the substrate (k_{sub}) and one connecting it to neighboring ligands (k_{link}) (Fig. 2a). For each ligand, its force F_i and displacement from rest position x_i were then calculated as:

$$F_i = k_{sub}x_i - k_{link}(x_i - x_{i-1}) + k_{link}(x_{i+1} - x_i)$$

At each time step, bound ligands were displaced by the amount of actin movement during the step (providing a known x_i), and unbound ligands were considered to be under zero load (providing a known F_i). This led to a system with n_l linear equations and n_l unknowns, corresponding to the forces of bound ligands and the positions of unbound ligands. After resolving the system, the total force exerted by all ligands was calculated. The degree of mechanical coupling between ligands (modelled by k_{link}) will depend on how forces are transmitted between nano-beads both through the cell cytoplasm and through the polyacrylamide gels. Those nanoscale parameters are essentially inaccessible experimentally and thus k_{link} values were merely adjusted to fit the data. Importantly however, this approach correctly reproduced the fact that local forces will induce decreasing deformations as distance increases. To take into account that the overall stiffness of the system depends on both k_{sub} and k_{link}, we used them to calculate an effective network constant k_{net}, corresponding to the spring constant obtained when pulling on one ligand connected to the entire network. k_{net} was calculated as an iterative process as:

$$k_i = k_{sub} + ((k_{link})^{-1} + (k_{sub})^{-1})^{-1} \qquad \text{for } i = 2$$

$$k_i = k_{sub} + ((k_{link})^{-1} + (k_{i-1})^{-1})^{-1} \qquad \text{for } 3 \le i \le n_l/2 - 1$$

$$k_{net} = k_{sub} + 2\left((k_{link})^{-1} + \left(k_{n_l/2\,-\,1}\right)^{-1}\right)^{-1} \qquad \text{for } i = n_l/2$$

The factor 2 in the last expression corresponds to considering the ligands both to the right and to the left of the one being pulled. Whereas this calculation corresponds to the ligand at the center of the system, we note that with the parameters used k_{net} quickly converged and was largely independent of either n_l or ligand position within the system. This k_{net} was then

used to calculate an equivalent substrate Young's modulus by assuming a characteristic adhesion radius r_0 as previously described[21,41]. The same characteristic radius was used to convert the one-dimensional model output of force into tractions (force per unit area).

Model parameters and predictions. All model parameters are described in Extended Data Table 1 along with their origin. The same base set of parameters was used to model all conditions, and the different conditions were modelled by modifying only the relevant parameters in the relevant direction. Specifically, the effect of increased ligand spacing was modelled by decreasing the number of clutches n_l, and the coupling between ligands k_{link}. More precisely, both k_{sub} and k_{link} scaled with rigidity, and to model ligand spacing we altered their ratio (k_{link}/k_{sub}). The effect of disorder was modelled by introducing a different value of k_{link} to each clutch rather than a constant value. Following the long-tailed distribution of distances observed in Extended Data Fig. 4, the values of k_{link} were chosen to be randomly distributed according to a Poisson distribution with a peak corresponding to the value employed in the ordered simulations. Of note, using a Gaussian rather than Poisson distribution led to the same relative trends. Regarding model predictions, those concerning adhesion formation and the effect of ligand distribution are discussed in the main text. However, an interesting point to add is that of the two parameters modified in the simulations (n_l and k_{link}/k_{sub}), n_l is the one responsible for shifting the optimal stiffness for adhesion formation, confirming previous analyses[22,23]. k_{link}/k_{sub}, in contrast, serves to modulate the height of the peak. With respect to stiffness and force/actin flow predictions, those have been discussed extensively in previous work[14,21,24]. Briefly, in the absence of adhesion reinforcement and recruitment, the molecular clutch model predicts a biphasic force/stiffness relationship, in which forces first increase and then decrease with rigidity. The introduction of force-dependent reinforcement triggers adhesion growth and force increase above a rigidity threshold, reverting the downward force trend predicted at high rigidities. Depending on the specific threshold, reinforcement can eliminate the high rigidity downward trend completely if the threshold is low (leading to a monotonically increasing force/rigidity curve) or only partially. In this case, the force/rigidity curve first increases, then plateaus or even decreases slightly, and then increases again due to reinforcement. Both cases are observed in this work: in ordered configurations (Fig. 2), the plateau is observed. In disordered configurations (Fig. 3), the threshold is shifted to lower rigidities and a monotonic curve is observed.

Data availability: The datasets generated during and/or analysed during the current study are available from the corresponding author on reasonable request

34 Allen, M. D. *et al.* Altered microenvironment promotes progression of preinvasive breast cancer: myoepithelial expression of alphavbeta6 integrin in DCIS identifies high-risk patients and predicts recurrence. *Clinical cancer research : an official journal of the American Association for Cancer Research* **20**, 344-357, doi:10.1158/1078-0432.CCR-13-1504 (2014).

35 Roca-Cusachs, P. *et al.* Integrin-dependent force transmission to the extracellular matrix by alpha-actinin triggers adhesion maturation. *PNAS* **110**, E1361-E1370, doi:1220723110 [pii];10.1073/pnas.1220723110 [doi] (2013).

36 Alcaraz, J. *et al.* Microrheology of human lung epithelial cells measured by atomic force microscopy. *Biophysical journal* **84**, 2071-2079, doi:10.1016/S0006-3495(03)75014-0 (2003).

37 Hutter, J. L. & Bechhoefer, J. Calibration of atomic-force microscope tips. *Review of Scientific Instruments* **64**, 1868-1873, doi:doi:http://dx.doi.org/10.1063/1.1143970 (1993).
38 Sengupta, P., Jovanovic-Talisman, T. & Lippincott-Schwartz, J. Quantifying spatial organization in point-localization superresolution images using pair correlation analysis. *Nature protocols* **8**, 345-354, doi:10.1038/nprot.2013.005 (2013).
39 Veatch, S. L. *et al.* Correlation functions quantify super-resolution images and estimate apparent clustering due to over-counting. *PLoS One* **7**, e31457, doi:10.1371/journal.pone.0031457 (2012).
40 Kong, F., García, A. J., Mould, A. P., Humphries, M. J. & Zhu, C. Demonstration of catch bonds between an integrin and its ligand. *The Journal of cell biology* **185**, 1275-1284, doi:10.1083/jcb.200810002 (2009).
41 Ghibaudo, M. *et al.* Traction forces and rigidity sensing regulate cell functions. *Soft Matter* **4**, 1836-1843, doi:10.1039/b804103b (2008).
42 Molloy, J. E., Burns, J. E., Kendrick-Jones, J., Tregear, R. T. & White, D. C. Movement and force produced by a single myosin head. *Nature* **378**, 209-212, doi:10.1038/378209a0 (1995).
43 Chan, C. E. & Odde, D. J. Traction dynamics of filopodia on compliant substrates. *Science* **322**, 1687-1691 (2008).
44 Litvinov, R. I. *et al.* Resolving two-dimensional kinetics of the integrin alphaIIbbeta3-fibrinogen interactions using binding-unbinding correlation spectroscopy. *J. Biol. Chem.* **287**, 35275-35285, doi:10.1074/jbc.M112.404848 (2012).
45 Kong, F., Garcia, A. J., Mould, A. P., Humphries, M. J. & Zhu, C. Demonstration of catch bonds between an integrin and its ligand. *J. Cell Biol.* **185**, 1275-1284 (2009).
46 Roca-Cusachs, P., Iskratsch, T. & Sheetz, M. P. Finding the weakest link - exploring integrin-mediated mechanical molecular pathways. *J.Cell Sci.* **125**, 3025-3038, doi:jcs.095794 [pii];10.1242/jcs.095794 [doi] (2012).

Extended data figures

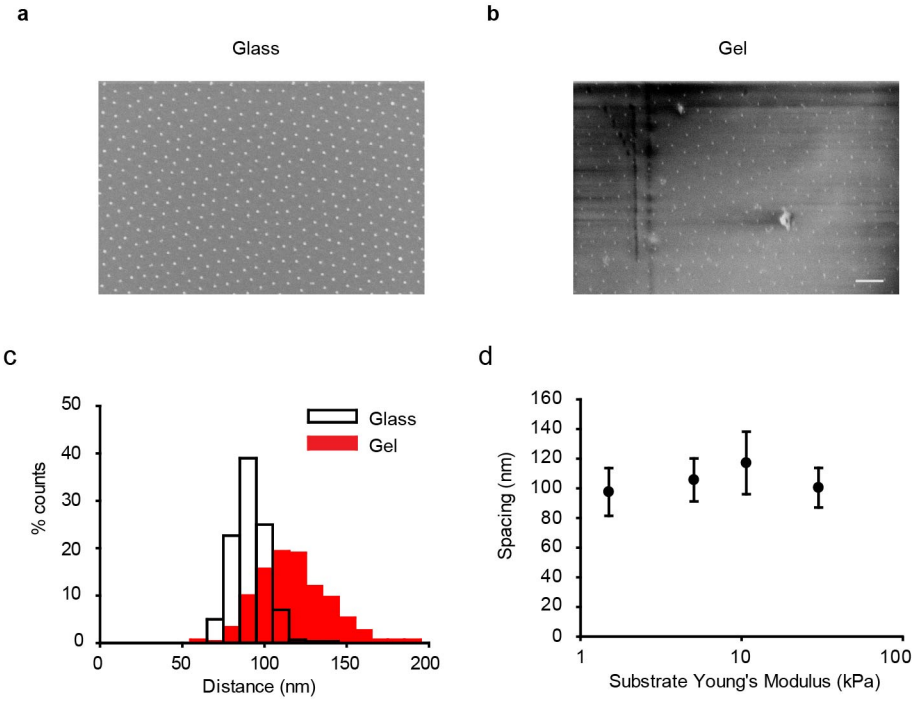

Extended Data Figure 1. Nanopattern swelling on gels. (a) Scanning electron micrograph of a quasi-hexagonal 100nm ordered pattern on a glass surface (2 independent experiments). (b) Scanning electron micrograph of a quasi-hexagonal 100nm ordered pattern on a polyacrylamide gel. (c) Corresponding histograms showing the distribution of distances between nano-dots and their first-order neighbors on glass and polyacrylamide substrates of 30 kPa (300 particles, two independent experiments). (d) Corresponding quantification of mean distance for polyacrylamide gels as a function of rigidity (n=300 particles per condition, two independent experiments). Scale bar, 100 nm.

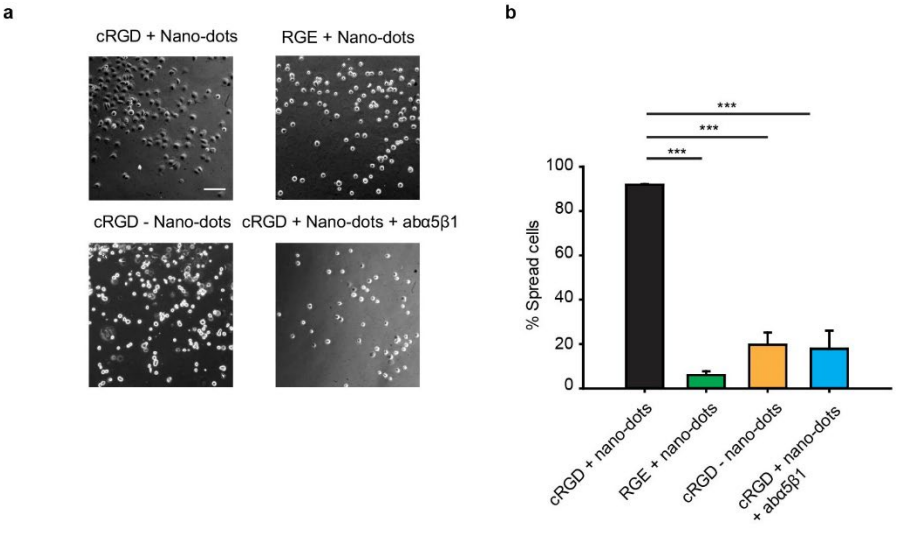

Extended Data Figure 2. Cell binding to nano-patterned substrates is specific to α5β1 integrins, cRGD, and nano-dots. (a) Images showing breast myoepithelial cells plated on 30kPa substrates with 50nm spacing for positive condition (cRGD+nano-dots), and negative conditions: nano-dots coated with negative peptide (RGE + nano-dots), cRGD incubated with gels without nanodots (cRGD – nano-dots) and cells incubated with an α5β1 blocking antibody plated on cRGD + nano-dots substrates (cRGD + ab α5β1. (b) Corresponding quantification of % spread cells (n=30/30/30/22 fields of view, 3 independent experiments). Scale bar, 100 μm. ***, p< 0.001. Error bars, mean ± s.e.m.

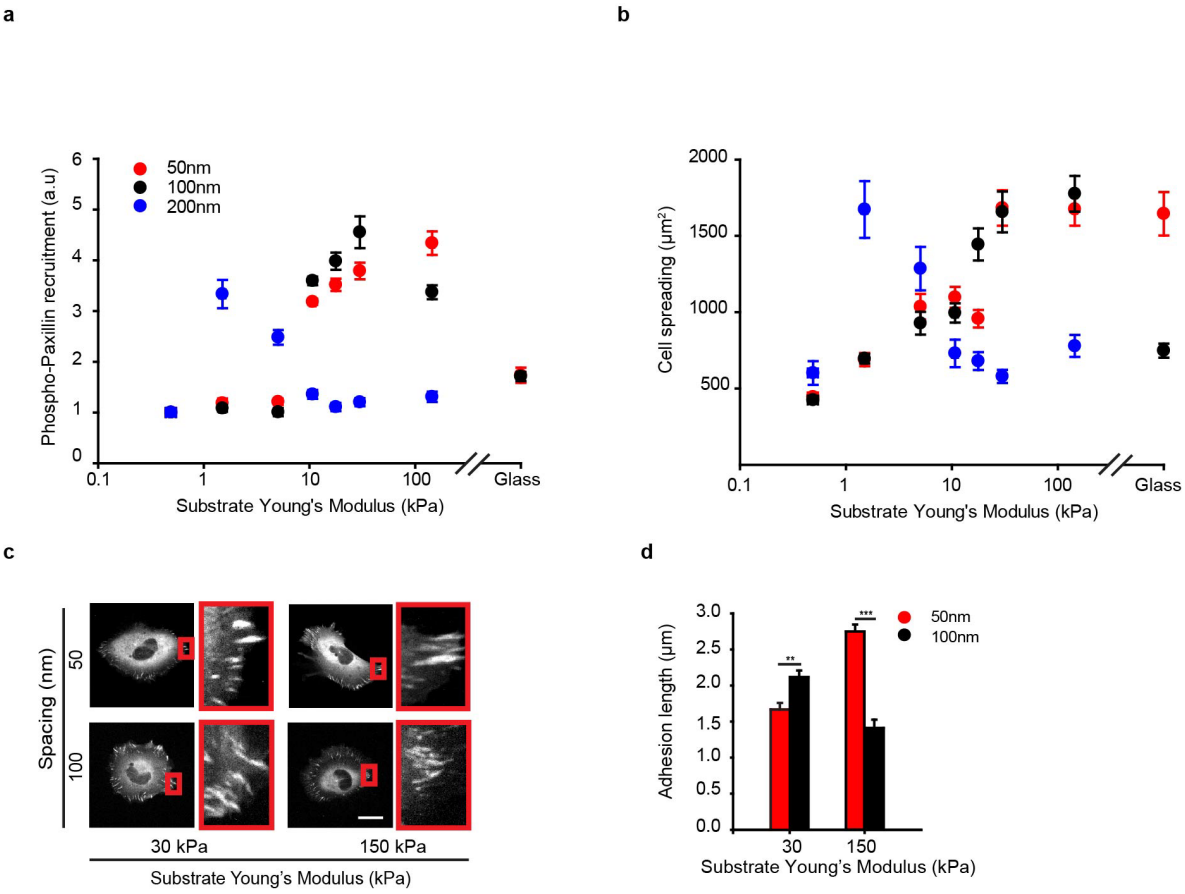

Extended Data Figure 3. Additional characterizations of cell response to rigidity and nano-dot spacing. (a) Quantification of the fluorescence intensity of phospho-paxillin stainings at the cell edge (two different regions per cell, n=10/10/11, 10/10/11, 10/11/11, 10/10/11, 10/10/11, 10/10/11, 10/10/11, 10/10/11 cells for 50/100/200 nm substrates and increasing rigidity, two independent experiments). The effect of both ligand spacing and rigidity was significant ($p<0.05$, two-way ANOVA). Rather than measuring FAs, this complementary measurement integrates phospho-paxillin recruitment in both adhesions and surrounding areas. The same trends were observed as in fig. 1e. (b) Cell spreading area (n=13/13/11, 11/16/11, 11/19/11, 16/13/11, 13/16/11, 13/14/11, 13/13/11 cells for 50/100/200 nm substrates as rigidity increases, two independent experiments). Whereas nano-dot spacing did affect cell spreading, we note that in 50 and 100 nm spaced substrates, the rigidities inducing adhesion formation and collapse are not associated with changes in cell spreading. (c) Examples of GFP-Paxillin transfected cells seeded on 30kPa and 150kPa substrates with 50nm and 100nm spaced patterns. Zoomed regions on the right of the images correspond to rectangles marked in red in the main image. (d) Corresponding quantification of FA length (10 adhesions per cell, n=11/11, 10/10 cells for 50/100 nm substrates as rigidity increases, two independent experiments) **, $p< 0.005$, ***, $p< 0.001$, two-way ANOVA. Scale bar, 20 μm. Error bars, mean ± s.e.m.

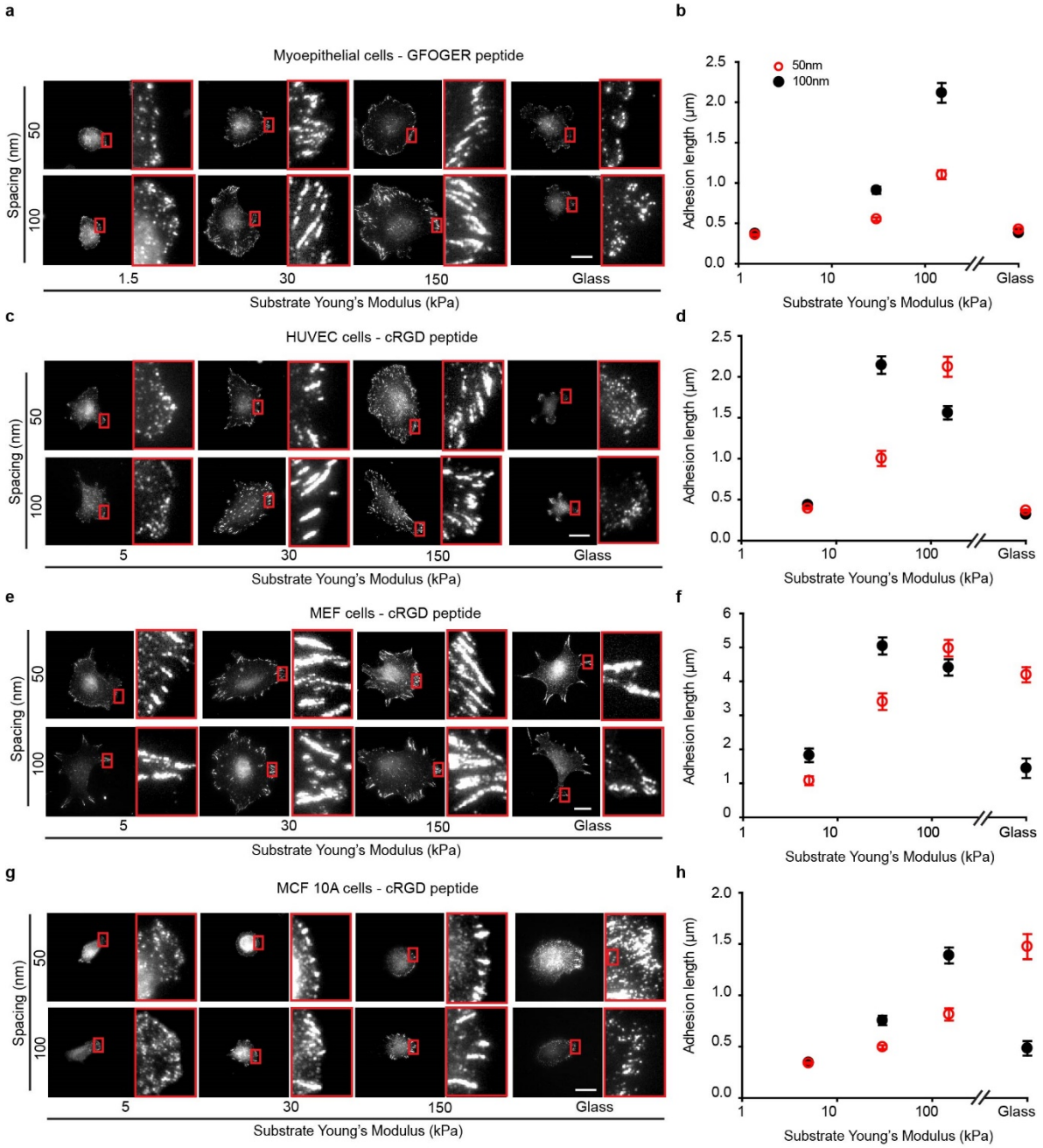

Extended Data Figure 4. Effect of rigidity and nano-dot spacing on different cell types and ligands. (a) Staining of phospho-paxillin adhesions of myoepithelial cells seeded on polyacrylamide substrates of different rigidities and glass with either 50 or 100nm spaced nano-dots coated with the collagen mimicking GFOGER peptide. Zoomed regions on the right of the images correspond to rectangles marked in red in the main image. (b) Corresponding quantification of FA length (at least 3 FA for n=15 cells per condition, two independent experiments). (c-h) Same as a-b for different cell types seeded on cRGD-coated nano-dots (c-d, HUVEC, e-f, MEFs, g-h, MCF10A). In all cases, at least 3 FA per

cell. For 50/100 nm substrates and increasing rigidity, n=16/16, 16/15, 15/16, 15/15 cells (HUVEC), n=15/15, 16/15, 15/15, 14/14 cells (MEFs), and n=15/15, 15/15, 15/15, 10/10 cells (MCF10A), two independent experiments. Scale bars, 20 μm. Error bars, mean ± s.e.m.

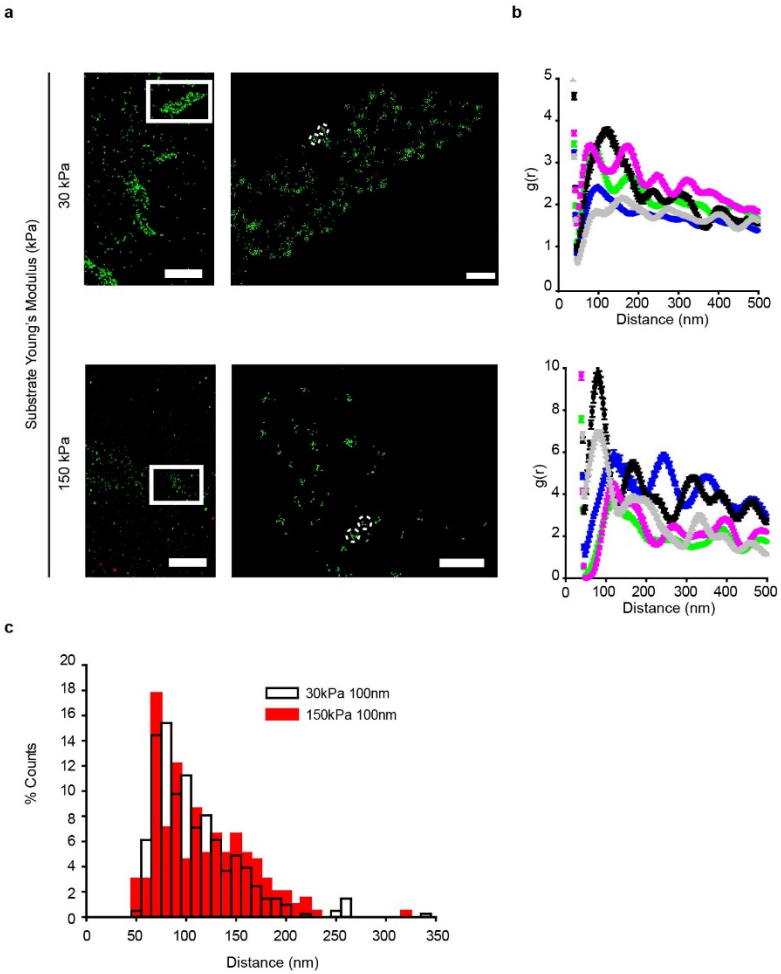

Extended Data Figure 5. Adhesion collapse is not associated with changes in nano-spacing between paxillin clusters. (a) STORM super-resolution images of phospho-paxillin stainings in cells seeded on 100 nm spaced patterns on 30 or 150 kPa gels. Left, overview image of different FAs. Scale bar, 5 µm. Right, zoomed images of the FAs marked in white in the left image. White circles show examples of phospho-paxillin clusters. Scale bar, 300 nm. 2 independent experiments. (b) Pair correlation functions of phospho-paxillin clusters as a function of distance in different adhesions (marked with different colors). In all cases, a first peak is observed around 100 nm, indicating the periodicity of the cluster pattern. (c) Histogram showing the distances between neighboring phospho-paxillin clusters (n= 409 and 197 clusters for 30 and 150 kPa respectively, two independent experiments). No significant differences were observed.

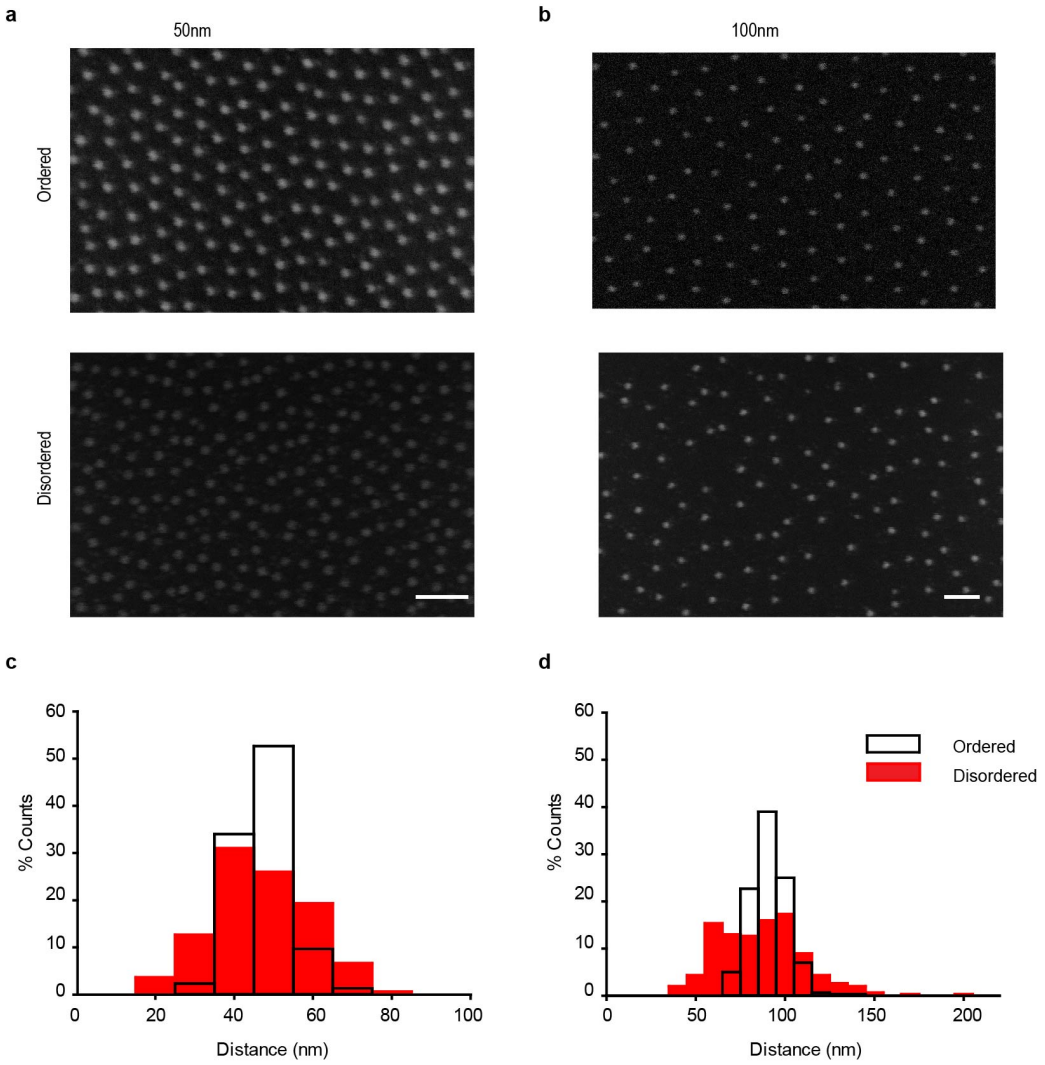

Extended Data Figure 6. Spatial distribution of ordered and disordered nanopatterns. (a-b) Scanning electron micrograph of ordered and disordered nanopatterns on glass for spacings of 50 nm (a) and 100 nm (b). Two independent experiments. (c-d) Histograms showing the distribution of interparticle distances for ordered and disordered patterns for 50 (c) and 100nm (d) (n=300 partciles for all the conditions measured in two independent experiments). Scale bar, 100 nm.

Parameter	meaning	Value	Origin
n_m	Number of myosin motors	190	Adjusted
F_m	Myosin motor stall force	2 pN	[42]
v_u	Unloaded myosin motor velocity	90 nm/s	Values measured here and [43]
n_l	Number of ligands (cRGD-functionalized nano-dots)	180 (50 nm) 130 (100 nm) 5 (200 nm)	Adjusted
d_{int}	Initial integrin density on the membrane	300/μm^2	[21]
d_{intmax}	Maximum integrin density on the membrane	2200/μm^2	Adjusted
K_{ont}	True binding rate	2.31x10^{-4} um^2/s	Adjusted, of the order of values reported for αIIBβ3[44]
K_{off}	Unbinding rate, scaling factor applied to force curve reported in [45]	0.5	Adjusted, catch bond dependency from [45]
$F_{threshold}$	Threshold reinforcement force	87 pN	Adjusted, of the order of reported values[46]
d_{add}	Integrins added after each reinforcement event	120/μm^2	Does not affect model output
a	Radius of adhesion	750 nm	Adjusted
k_{link}/k_{sub}	Elastic coupling between ligands	10 (50 nm) 5 (100 nm) 3 (200 nm)	Adjusted

Extended Data Table 1. Model parameters.

Generated structures	Styrene units (x)	Vinyl-pyridine units (y)	c in mg/ml	Loading parameter of $HAuCl_4$	Spin coating speed in rpm
200 nm ordered	5348	713	2	0.5	11000
100 nm ordered	1824	523	4	0.6	10000
100 nm disordered	a) 1824 b)123000	523	4 8	0.5	8000
50 nm ordered	1056	495	8	0.5	7000
50 nm disordered	a) 1056 b)50 000	671	9 8	0.3	5000

Extended Data Table 2. Preparation details on micellar nanolithography.

In disordered structures, a) and b) refer to micellar and polystyrene solutions, respectively.

% Acrylamide	% Bis-Acrylamide	Young's Modulus (kPa) Mean ±s.e.m.)	Number of gels
4	0.03	0.49±0.05	6
5	0.04	1.50±0.09	6
7.46	0.044	5.06±0.13	6
7.5	0.1	10.72±0.71	6
7.55	0.16	17.76±0.67	6
12	0.15	30.02±0.56	6
12	0.6	144.88±6.6	6

Extended Data Table 3. Polyacrylamide gel rigidities measured with AFM.